Measurement of propagation constant in waveguides with wideband coherent terahertz spectroscopy

Sillas Hadjiloucas

Department of Cybernetics, The University of Reading, Whiteknights, Reading, RG6 6AY, UK

Roberto K. H. Galvão

Divisão de Engenharia Eletrônica, Instituto Tecnológico de Aeronáutica, São José dos Campos, SP, 12228-900, Brazil

John W. Bowen

Department of Cybernetics, The University of Reading, Whiteknights, Reading, RG6 6AY, UK

Rainer Martini, Martin Brucherseifer, Harm P. M. Pellemans, Peter Haring Bolívar, and Heinrich Kurz

Institut für Halbleitertechnik, Rhejnisch Westfalische Technische Hochschule Aachen Sommerfeldstrasse, 52056 Aachen, Germany

John Digby and Geoffrey M. Parkhurst

Department of Physics, University of Nottingham, Nottingham NG7 2RD, UK

J. Martyn Chamberlain

Department of Electronic and Electrical Engineering, The University of Leeds, Leeds, LS2 9JT, UK

Received February 22, 2002; revised manuscript received July 14, 2002

A quasi-optical technique for characterizing micromachined waveguides is demonstrated with wideband time-resolved terahertz spectroscopy. A transfer-function representation is adopted for the description of the relation between the signals in the input and output port of the waveguides. The time-domain responses were discretized, and the waveguide transfer function was obtained through a parametric approach in the z domain after describing the system with an autoregressive with exogenous input model. The *a priori* assumption of the number of modes propagating in the structure was inferred from comparisons of the theoretical with the measured characteristic impedance as well as with parsimony arguments. Measurements for a precision WR-8 waveguide-adjustable short as well as for G-band reduced-height micromachined waveguides are presented.

OCIS codes: 230.7370, 300.6270, 350.4010, 320.5540, 310.6870.

1. INTRODUCTION

At microwave frequencies, measurements of the scattering parameters, attenuation coefficients, and characteristic impedances of waveguide components are performed with four- or six-port network analyzers.[1–5] In such measurements, the most common calibration item is the precision air–dielectric coaxial transmission line or air line, although some calibration techniques have also been described with an attenuator as a calibration item.[6–10] Network analyzers are calibrated with at least three known terminations, and the characteristic impedance is conventionally determined with reference to a standard impedance line. In two-port network analyzers, through-reflect-line or line-reflect-line measurements,[11,12] in which the line standard is placed between the two ports, are used for calibration purposes, whereas in reflectometers, air lines in conjunction with terminations as calibration items are used. However, as the frequency is increased to 100 GHz, very few manufacturers can provide vector measurement capability, the waveguide samples become smaller, and the repeatability of the measurement becomes increasingly dependent on the ability of the user to couple sufficient power to the waveguide ports and to accurately measure the power ratios between the analyzer's ports under different calibration conditions.[13–15] Furthermore, the manufacture of precision reference terminations becomes difficult. At these higher frequencies, a quasi-optical approach for building instruments with high-density polyethylene lenses and mirrors that control the diffractive spreading of the beam offers significant ad-

vantages such as very low loss, multioctave operation, and noncontact coupling to the test ports.[16–18]

Generally, it is possible to quasi-optically measure the scattering matrix (S parameters) of a two-port device under single-mode excitation with a null-balance bridge reflectometer and a de-embedding procedure.[19] Because the position of the focusing elements in a quasi-optical instrument must remain fixed during a set of measurements, as would be necessary to measure a range of waveguide lengths, the distance between the feed antennas, and consequently the degree of coupling to the test beams, would be different for each test piece, causing an error in the measured S parameters. Therefore a transmissometer cannot be implemented, and a reflectometer in conjunction with a one-port de-embedding procedure is used. This approach implies that the only requirement is ensuring that a constant separation and alignment is maintained between the reflectometer test port and the feed antenna on each test piece. Each one-port test piece is a length of waveguide terminated in a short and connected to the reflectometer by a two-port device consisting of a further length of waveguide, the feed antenna, and any additional optics necessary to improve coupling between the reflectometer and the feed antenna.

In a previous study,[20] we used a continuous-wave (cw) broadband source coupled to a polarizing Martin–Puplett dispersive Fourier-transform spectrometer (DFTS) operated in reflectance mode to measure the characteristic impedance in waveguides when these were shorted at different lengths. The limited signal-to-noise ratio of our system, however, did not permit us to report propagation-constant measurements at that time. Time gating was used to separate the individual reflection signatures of the device under test from those of the antenna–lens system which formed the measurement port of the spectrometer. The procedure is equivalent to the frequency-sweeping process with a vector network analyzer, the only difference being that it is performed directly in the time domain, and thus the need for the extra Fourier transform necessary for time gating is obviated. Furthermore, the use of two known waveguide lengths, with the shortest length used to provide a background interferogram, implies that the whole process is directly referenced to the impedance of free space provided by the reference arm in the interferometric spectrometer and that no other reference calibration standard is required. In this paper, in order to circumvent the limited power output of the mercury-arc lamp used in cw DFTS, an alternative quasi-optical technique for characterizing terahertz (THz) micromachined waveguides[21] is proposed using identical waveguides of different lengths and wideband coherent terahertz spectroscopy. Our one-port approach differs from the two-port approach reported by Grischowski's group.[22–27]

A difficulty that arises when conventional time-domain terahertz spectroscopy is used for the characterization of waveguides intended for operation near 100 GHz is that most of the power output from the wideband pulsed source occurs at frequencies (e.g., 1–3 THz) where the waveguide can support a number of modes. The power output over the single-mode bandwidth of the waveguide is often rather low, leading to a poor signal-to-noise ratio there. At frequencies where multimode propagation can occur, a meaningful analysis is only possible if the extent to which each waveguide mode has been excited is known. This paper introduces a combination of wavelet-filtering and system-identification techniques to improve the signal-to-noise ratio and to characterize the multimode propagation.

2. EXPERIMENTAL SETUP

The experimental setup for generating and detecting THz radiation is shown in Fig. 1. A 76-MHz repetition-rate mode-locked Ti:sapphire laser producing optical pulses with durations of ~140 fs is used to resonantly excite (with an excitation power of 270 mW) the lowest interband transitions of an InGaAs emitter that is located at the focal point of a parabolic reflector.[28,29,30] The optical pulse generates an electron–hole plasma, and the accelerated carriers generate a pulse of THz radiation that is horizontally polarized along the direction of the surface field of the InGaAs emitter. THz pulses emitted by the photoconductive element are transmitted through a vertical 10-μm center-to-center spacing free-standing tungsten-wire polarizing beam-splitter grid. The propagating THz beam, which has a Gaussian transverse amplitude distribution, is focused by the second parabolic mirror to feed at normal incidence, in a copolar manner, the open port of the waveguide under test. The optics are designed to give frequency-independent coupling at the test port. The function of the second polarizing grid at +45° with respect to the horizontal is to ensure that only the linearly polarized component of the pulse at −45° with respect to the horizontal is transmitted. Upon 180° reflection at the backshort, the modified terahertz pulse exits the waveguide and is retransmitted through the 45° grid in a time-reversed manner, the vertically polarized component being reflected by the vertical grid and focused with a parabolic mirror to a time-gated (28-mW gate-power, 1-μA photocurrent) ion-implanted silicon-on-sapphire photoconductive dipole antenna.[31] Such a configuration permits measurements to be performed at exactly normal incidence (with respect to the azimuth) to the device under test, which is important in order to prevent measurement artifacts that can occur when a slightly divergent input and output beam configuration is used. Additionally, the high cross-polar levels originating from the focusing action of the paraboloids are suppressed to levels governed by the cross-polar performance of the grids, in order to allow a precise analysis of polarization dependencies. However, there is a power penalty, as only 1/4 of the emitted THz power is used for the measurements. An interesting feature of the experimental setup is that the Ti:sapphire laser pulses used to excite the photoconductive switch are in the visible part of the spectrum and co-propagate with the THz beam. This ensures that the focal point of the paraboloid, which is similar for both the visible and the THz pulses, can be easily identified. This proves useful for an initial coarse alignment of the test piece with the THz beam. Further optimization of the coupling between the waveguide structures under test and the THz E-field was ensured by minimizing the magnitude of the reflected pulse at the en-

trance of the structure. A microscope fitted with a vernier scale in the eyepiece and a five-axis translational/rotational stage were used for the final alignment procedure. The procedure ensured high repeatability in the measurements.

One sequence of measurements was performed on a commercially available precision WR-8 waveguide-adjustable short. The time-domain interferograms shown in Fig. 2(a), corresponding to five different positions of the adjustable backshort at 1-mm spacings, were recorded with a lock-in amplifier ($\tau = 300$ ms) after coaveraging three scans (1000 measurements per step with 100-ms wait states). The small oscillations at 0 mm in Fig. 2(a) are due to the impedance mismatch between the waveguide and free space. Use of an adjustable short to provide different test waveguide lengths ensured that a constant degree of coupling was maintained between the THz beam and the test piece throughout the measurement sequence.

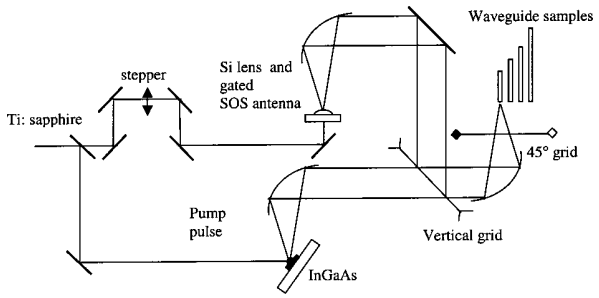

Fig. 1. Experimental setup for waveguide characterization.

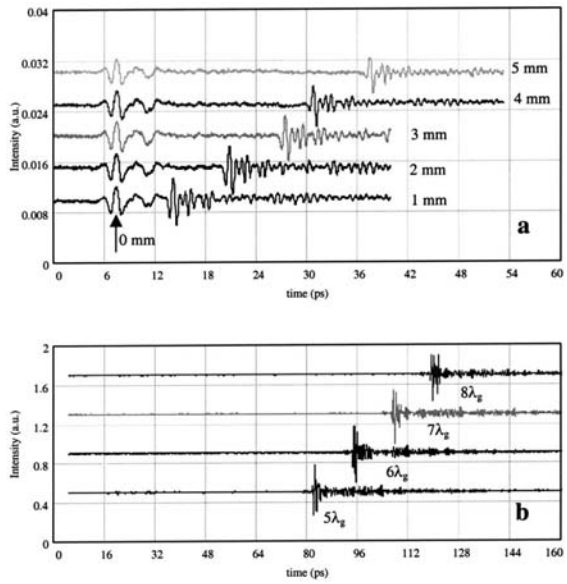

Fig. 2. (a) Time-domain reflection signatures for five different WR-8 waveguide lengths 1 mm apart and (b) for four reduced-height micromachined waveguides $5\lambda_g$, $6\lambda_g$, $7\lambda_g$, and $8\lambda_g$ long.

Fig. 3. Photograph of micromachined waveguide with antennas at both ends.

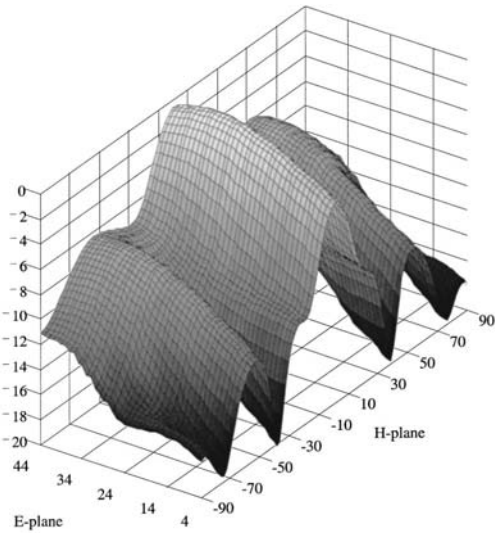

Fig. 4. Copolar far-field patterns for the integrated antenna at 197 GHz.

In another sequence of measurements, the time-domain signatures for four lengths of G-band (140–220 GHz) 1300 $\mu m \times 80$ μm micromachined[21] reduced-height waveguide were recorded [Fig. 2(b)] after sequentially placing them at the test port of the interferometer with the alignment procedure described earlier. The test pieces, which differed from each other by a unit length of 1.83 mm, were coupled to the beam with nominally identical integrated reduced-height slotted horn antennas flared in the *H* plane. The cutting of an exponentially tapered slot from the upper surface of the basic *H* plane sectoral horn (Fig. 3) resulted in a design that did not suffer the disadvantage of a restricted aperture height. Although the design implied that the beam would be astigmatic, adjustment of the horn parameters (flare angle, aperture width, slot angle, and position of the slot apex relative to the start of the horn flare) had been performed to produce a pattern with reasonable *E*- and *H*-plane beam widths. The far-field pattern of this antenna has been previously characterized in the 150–200-GHz frequency range (single-mode operation), showing an elevation of 34° at the *E* plane for optimal coupling (Fig. 4). The THz pulse produced by the photoconductive antenna has frequency components up to 3 THz.

3. SYSTEM IDENTIFICATION WITH AN AUTOREGRESSIVE WITH EXOGENOUS INPUT MODEL

The use of parametric models to obtain a filtered version of the Fourier-transformed signal has been already re-

ported in the past.[32–34] In this paper, however, we propose the use of a parametric input/output model and an identification procedure to obtain the frequency response of a waveguide test piece. Ratioing the measured spectra $U(j\omega)$ and $Y(j\omega)$ for the shorter (one-unit length) and longer (two-unit lengths) waveguides, respectively, should result in the effective complex insertion loss function $H(j\omega)$ for a unit-length d (double-pass) waveguide with a 180° phase shift due to the reflection at the backshort. This can be interpreted in the following manner. With reference to Fig. 5, let $P(j\omega)$ be the Fourier transform of the excitation pulse, which is supposed to be the same for all experiments. This is a reasonable assumption, since signals acquired with a lock-in technique are coaveraged after several pulses, thus reducing the effect of pulse-to-pulse variability. In addition, let $G_1(j\omega)$ and $G_2(j\omega)$ be the frequency responses of the antenna section coupling the pulse into the shorter and longer waveguides, respectively. Since the antenna–waveguide structure is a reciprocal device, it is possible to write

$$U(j\omega) = H(j\omega){G_1}^2(j\omega)P(j\omega), \tag{1}$$

$$Y(j\omega) = H^2(j\omega){G_2}^2(j\omega)P(j\omega). \tag{2}$$

Such a model formulation is valid as long as the electrical size of the antenna tapers slowly, ensuring a smooth transition between the waveguide structure and free space, or can be gated out, so that Fabry–Perot effects of the reflected pulse need not be taken into account (Appendix A). This is usually the case when either the structure is nondispersive or when the structure is long enough. Close inspection of the time-domain signatures in Fig. 2 showed that this formulation was adequate for our data set, since if there were such Fabry–Perot effects in the devices under test, multiple reflection signatures of gradually lower magnitude would have been identifiable at distances given from $4\bar{n}d/c$ (where $\bar{n}$ is the effective refractive index of the waveguide structure of length d assuming multimode propagation and c is the speed of light in vacuum). Ratioing $Y(j\omega)$ with $U(j\omega)$ after assuming that the difference between $G_1(j\omega)$ and $G_2(j\omega)$ is negligible, yields $H(j\omega)$, that is

$$H(j\omega) = \frac{Y(j\omega)}{U(j\omega)}. \tag{3}$$

Notice that the complex insertion loss $H(j\omega)$ can be regarded as the frequency response of a linear system that produces an output $y(t)$ for an input $u(t)$, where y and u are the measured time-domain responses. In this manner, it is possible to obtain $H(j\omega)$ through a parametric approach, in which the system is described by an autoregressive with exogenous input (ARX) model of the form

$$\begin{aligned} y[k] + a_1 y[k-1] + \ldots + a_{n_a} y[k-n_a] \\ = b_1 u[k-n_k] + b_2 u[k-n_k-1] \\ + \ldots + b_{n_b} u[k-n_k-n_b+1] + \epsilon[k], \end{aligned} \tag{4}$$

where $y[k]$ is the response measured at time kT_s and $\{a_1,\ldots,a_{n_a}, b_1,\ldots,b_{n_b}\}$ are model coefficients, n_a is the number of poles (equivalent to the system order), $(n_b - 1)$ is the number of zeros, n_k is a pure time delay, and $\epsilon[k]$ is a residual, which is to be minimized by the identification process. Hence $H(j\omega)$ can be obtained from the discretized z-domain transfer function $H(z)$ given by

$$\begin{aligned} H(z) = \frac{Y(z)}{U(z)} &= z^{-n_k}\frac{b_1 + b_2 z^{-1} + \ldots b_{n_b} z^{-n_b+1}}{1 + a_1 z^{-1} + \ldots a_{n_a} z^{-n_a}} \\ &= z^{-n_k}\frac{N(z)}{D(z)}. \end{aligned} \tag{5}$$

The frequency response can be obtained from the z-domain transfer function by making $z = \exp(j\omega T_s)$, where T_s is the sampling time (27 fs for the backshort data and 3.6 fs for the micromachined waveguide data). It is well known in linear-systems theory that the roots of $D(z)$ [termed poles of $H(z)$] are associated with the modes of the system. The roots of $N(z)$ [termed zeros of $H(z)$] are associated with the weights of each TE_{mn} mode in the overall response of the system ($n + m$ modes in total). In addition, $H(z)$ can be expanded (Appendix B) in the following partial fractions form:

$$H(z) = z^{-n_k}\sum_{i=1}^{n+m} w_i \frac{1 + f_i z^{-1}}{1 + c_{i1} z^{-1} + c_{i2} z^{-2}}, \tag{6}$$

where $n + m = n_a/2$ [since the order of the denominator of $H(z)$ is n_a and there are $n + m$ terms in the expansion, each one with a second order denominator]. Each partial fraction describes a propagating mode inside the waveguide. The ith mode will have weight w_i, a resonant frequency of oscillation ω_{ni}, and a damping ratio ζ_i given by the roots of the polynomial in the ith denominator. It is worth noting that this is the minimal representation needed to describe a mode, since the first-order term in the numerator of the partial fraction will account for the cut-on effect in the frequency domain, whereas the second-order term in the denominator will ensure that the response is attenuated at high frequencies. For modeling parsimony, no extra zeros or poles are incorporated in the description of each mode. Parameters a_i and b_i can be obtained by minimizing the mean-square value of the residual $\epsilon[k]$ over the time horizon used for identification (Appendix C), with a least-squares procedure.

When choosing the order of the model (that is, n_a), one can make an assumption on the number of modes that are propagating in the structure. It is convenient to make n_b equal to n_a ($n_a \geqslant n_b$ always for a causal system), which is the most general formulation for a given number of modes. The value of n_k can be accurately estimated after observing the time-domain signatures as recorded by setting the calibrated delay line of the spectrometer from

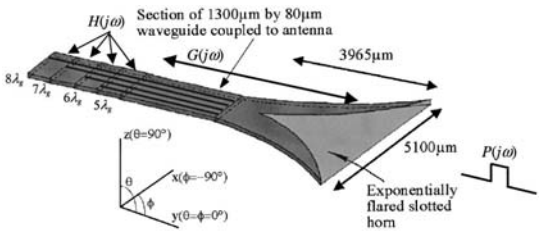

Fig. 5. Backshorted micromachined reduced-height waveguide structures of different lengths coupled to exponentially flared antenna structure, as used for the experiments.

$$\varphi(\omega) = \tan^{-1}[\mathrm{Im}(H(j\omega))/\mathrm{Re}(H(j\omega))]. \quad (7)$$

Careful observation of Eq. (5) above shows that it is equivalent to the more familiar equation of the complex insertion loss $\hat{H}(\omega)$ in dispersive Fourier-transform spectrometry[35]:

$$\hat{H}(j\omega) = H(\omega)\exp[-j\phi(\omega)], \quad (8)$$

where $\varphi(\omega) = z^{-n_k}|_{z=\exp(j\omega T_s)}$. The theoretical cut-off wavelength λ_c for each TE_{mn} mode that excites the rectangular waveguide structures is calculated from the known waveguide dimensions a, b by[36]

$$\lambda_{c_{mn}} = \frac{2\sqrt{ab}}{\sqrt{m^2\frac{b}{a} + n^2\frac{a}{b}}}. \quad (9)$$

The guide wavelength λ_g inside the waveguide can then be calculated for each mode from $\lambda_{g_{mn}} = \lambda/(1 - \lambda/\lambda_{c_{mn}})^{1/2}$, where λ is the wavelength in free space. The theoretical phase delay at each frequency for each mode is $\varphi_{mn} = \pi + 2\pi 2d/\lambda_{g_{mn}}$, where the length $2d$ corresponds to a double-pass measurement and the factor π arises from the reflection of the incident wave from the backshort in the waveguide. In order to calculate the overall phase, vectorial addition was performed for all the propagating modes inside the waveguide. Since each mode is attenuated to a different degree, its contribution must be weighted by a weight w_i and the attenuation constant α:

$$H(j\omega) = \sum_{i=1}^{m+n} w_i\{\exp[-\alpha_i(\omega)2d]\exp[j\varphi_i(\omega)]\}. \quad (10)$$

Figure 6(a) is a plot of the measured and theoretical phase differences $\Delta\varphi_m$ and $\Delta\varphi_{\mathrm{th}}$, respectively, for the five different WR-8 waveguide samples with the shortest sample as the zero phase reference and the consecutive waveguide lengths as samples. It can be observed that the measured slope for each consecutive waveguide length is an integral multiple of the slope of the shorter waveguide. The same procedure was followed for the reduced-height micromachined waveguides [Fig. 6(b)], where a unit length of $5\lambda_g$ was used for the background interferogram and successive waveguide lengths of $6\lambda_g$, $7\lambda_g$, and $8\lambda_g$ have been used as samples. This is in good agreement with the theoretical calculations, showing that the focused THz pulse couples well to the test port and excites the fundamental TE_{10} mode. This is a consequence of the focusing action of the parabolic reflector that preferentially couples to the TE_{10} mode as well as the filtering action of the grid to the modes that have a cross-polar component. Such a conclusion is further supported from calculations of theoretical phase delay assuming all modes up to 3 THz propagate through the structures and that there is equal power in each mode that deviates from the experimental values. The theoretical calculations imply that most of the power is distributed among two modes, and thus a fourth-order model should be adopted for the backshort experiment. In a similar manner, a sixth-order model corresponding to three waveguide modes was adopted for the analysis of the micromachined waveguide data.

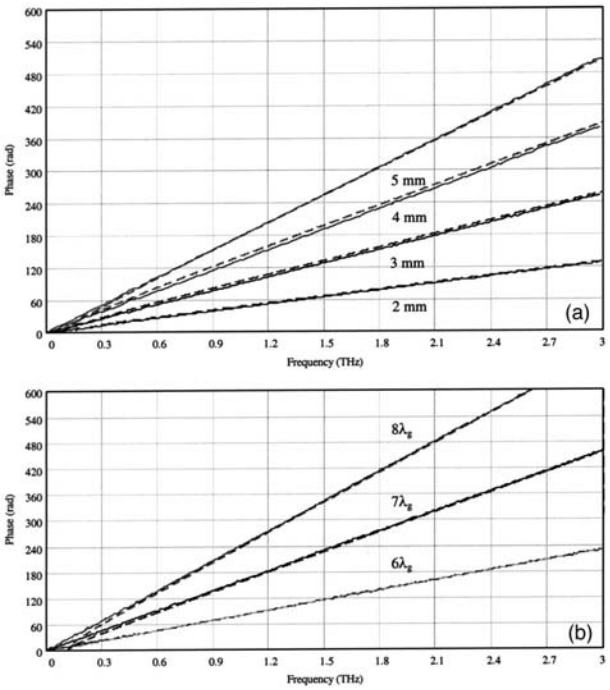

Fig. 6. (a) Consecutive phase measurements with the first backshort position (1 mm) used as a background interferogram and backshort positions at 2 mm, 3 mm, 4 mm, and 5 mm treated as samples; (b) phase measurements for reduced-height micromachined waveguides with the $5\lambda_g$ sample used for the background interferogram and consecutive lengths as samples. Dashed curves represent simulated results assuming the TE_{10} mode only propagating through the structure.

Careful examination of the phase velocity of the received signal for the WR-8 short as well as for the micromachined waveguides shows that the propagation of THz pulses inside the waveguide is almost dispersion free within the bandwidth of the excitation pulse, indicating that the micromachining technique employed in the construction of the waveguides is capable of producing internal waveguide surfaces with sufficiently fine tolerances to support frequencies well above 200 GHz. Such results are also in good agreement with the high-quality surface finish observed in TEM pictures.[21] It is worth noting that most recently,[25] Grischkowsky's group has also observed dispersion-free propagation of THz pulses in waveguide structures.

The *a priori* assumption on the number of modes propagating in the structure, as well as the hypothesis of exponential decay of each mode (energy dissipation), implies that the ARX model has a low-pass filtering effect in the original data set. This implies that using a parametric model to represent the waveguide has the added advantage of reducing the number of coefficients that need to be obtained. In fact, the process of ratioing spectra to obtain the complex insertion loss corresponds to identifying $N/2$ complex-valued Fourier coefficients, whereas in the identification procedure, only $n_a + n_b$ real-valued param-

eters are involved. This reduction in the number of descriptive elements results in an improvement in the confidence of the estimation, since the ratio between the number of experimental data to the number of unknowns increases. A parallel can be traced to the improvement in the signal-to-noise ratio that is enjoyed when the number of spectral bins is decreased with boxcar filtering. In this sense, the identification procedure can be regarded as a filtering process, which reduces the number of features to be estimated.

4. WAVELET-TRANSFORM FILTERING

Before the identification procedures, the signals were mean centered, and the wavelet transform was used for filtering. For this purpose, a decomposition with the db4 mother wavelet[37,38] with two scale levels was employed (Fig. 7). The wavelet transform of the discrete signal representing the reflection signatures in the time domain $f(t)$ with N points was written as

$$Wf(a, b) = \sum_{t=0}^{N-1} f(t)\psi_{a,b}(t), \tag{11}$$

where the wavelet function $\psi_{a,b}(t)$ was built from a mother wavelet function $\psi(t)$:

$$\psi_{a,b}(t) = \frac{1}{\sqrt{a}}\psi\left(\frac{t-b}{a}\right), \tag{12}$$

where subscript $a \in R^*$ is now the "scale" (or "dilation") that determines the width of the wavelet and subscript $b \in R$ defines the position of the wavelet in time. Parameters a and b were discretized in the following manner: $a = 2^j$, $b = j2^k$, where j and k are integer numbers. The transform result yields the discrete wavelet-transform coefficients, which are indexed by j (scale level) and k (translation index). A threshold of 0.01 times the largest wavelet coefficient was adopted in the filtering procedure, and the inverse wavelet transform was then employed. The effect of such filtering is shown in Fig. 8. The fast wavelet transform was implemented according to Mallat's filter-bank algorithm.[39] Wavelet filtering was preferred because it is known to yield better results than conventional filters (such as boxcar, moving average, Fourier, or dynamic filters) when the frequency content of the signal changes with time.[40–43] This is the case in our experiments, where some waveguide modes die out quicker than others.

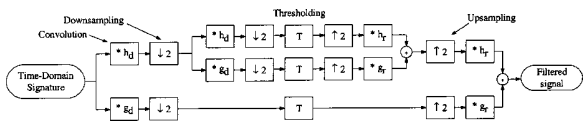

Fig. 7. Block diagram of the wavelet-transform filtering procedure. h_d and g_d are low-pass and high-pass decomposition filters, respectively, whereas h_r and g_r are their reconstruction counterparts.

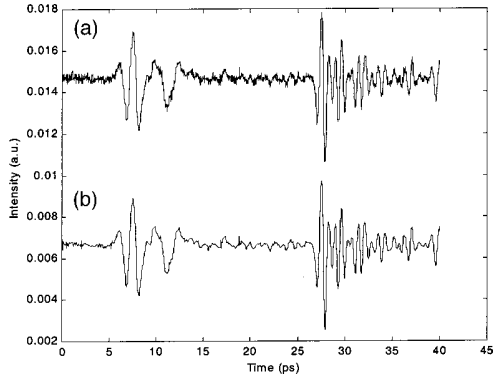

Fig. 8. (a) Original time-domain signature of the backshort and (b) the wavelet-transform filtered signal.

5. RESULTS

The System Identification Toolbox of Matlab 5.3 was used to obtain models in the form of Eq. (4). Figure 9(a) shows the insertion loss of a unit-length waveguide (as calculated by the ARX model) after ratioing the spectra obtained with the backshort adjusted to 3 mm with that at 2 mm. These results are similar to those obtained after ratioing spectra with the backshort positioned at 5 and 4 mm, respectively. Results corresponding to the effective insertion loss due to two unit lengths of waveguide are also shown. Taking into account the confidence levels (one sigma) of the identification procedure, the results shown in Fig. 9(b) are in agreement with the requirement that the measured insertion loss for a two-unit length waveguide should be equal to the squared value of that of a single-unit waveguide. The measured time-domain response and the predicted response with a fourth-order ARX model are in excellent agreement, as shown in Fig. 10. The observed increased insertion loss at higher frequencies is attributed to the variation of the conductivity of gold with frequency.

Figure 11(a) shows the autocorrelation values of the ARX modeling residual $\Sigma_k \epsilon[k]\epsilon[k-x]$, where x is a time shift between two points of the ARX residual sequence and Fig. 11(b) shows the cross correlation $\Sigma_k \epsilon[k]u[k-x]$ between the modeling residual and the input signal for different time shifts k. Ideally, the autocorrelation should be zero for delays different from zero (white noise), and there should be no cross correlation between the residual and the input, since any correlation would indicate that part of the residual could be predicted from the input. Since the autocorrelation of the residuals is small, the assumption of whiteness in the noise can be assumed to be valid. If colored noise were present, an autoregressive with moving average and exogenous input (ARMAX) model might provide a better description of the data.

Results for the micromachined waveguides after assuming that all the excitation energy is contained in three propagating modes are shown in Fig. 12(a). The insertion loss for one, two, and three waveguide lengths of micromachined waveguides is calculated after a $5\lambda_g$-long waveguide piece is used to record a background interferogram and $6\lambda_g$, $7\lambda_g$, and $8\lambda_g$ waveguide lengths as samples. The confidence levels (one sigma) of the identification procedure are also shown [Fig. 12(b)].

The pole-zero charts in Fig. 13 and Fig. 14 provide more details of the results obtained by the ARX model for

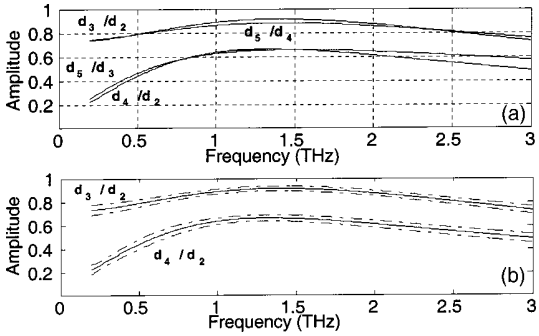

Fig. 9. (a) Calculated transmission coefficient of a unit-length and a two-unit-length waveguide for the backshort and (b) confidence levels (one sigma) of the identification procedure.

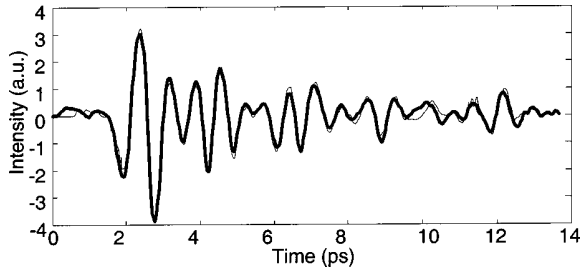

Fig. 10. Measured (thin curve) time-domain response for the d_3/d_2 case and predicted (thick curve) response with a fourth-order model.

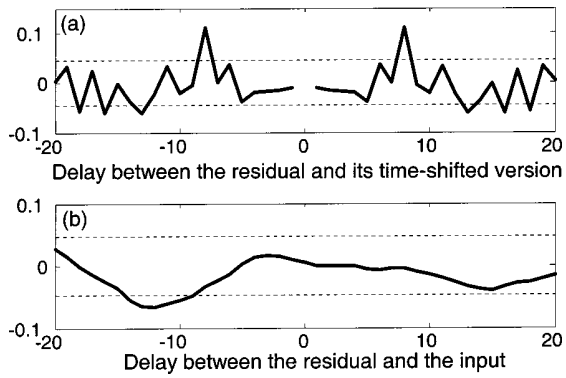

Fig. 11. Residual statistics for the d_3/d_2 case, with a fourth-order model. The autocorrelation values (a) of the modeling residual $\epsilon[k]$ and (b) the cross correlation between the modeling residual and the input signal. The dashed curves are the bounds of the region in which the residual statistics should be with a 68% confidence level (one sigma) for a conveniently chosen model structure.

the backshort and micromachined waveguide cases, respectively. The horizontal and vertical axes represent the respective real and imaginary parts of the poles and zeros in the complex plane. The dashed isoclines provide values of natural frequencies ω_n and damping ratios ζ for the propagating modes. The isoclines are obtained from

$$z = \exp[T_s(-\zeta\omega_n \pm j\omega_n\sqrt{(1-\zeta^2)}], \qquad (13)$$

where $0 \leqslant \zeta \leqslant 1$, $\omega_n \geqslant 0$ by fixing ζ and varying ω_n or by fixing ω_n and varying ζ. It is worth noting that the confidence locus of the zeros is much larger than the confidence locus of the poles. This was to be expected, since it is easier to estimate poles than zeros, as the former are associated with the exponential decay and frequency of oscillation of the modes, whereas the zeros are associated with the weights of each mode, which are intuitively more difficult to obtain. In addition, if more modes were assumed in the model, the radii of the confidence zones of the poles and zeros would increase, since the number of unknowns would be larger, for the same number of observations. The inset in Fig. 13 shows that the confidence levels in the model decrease significantly when the model is overparametrized. Since the autocorrelation function of the residual is within the one standard error bounds, it can be concluded that the model is appropriate to describe the data set.

Figure 14 shows a pole-zero chart depicting the three propagating modes described by the ARX model inside an antenna-coupled reduced-height waveguide when a waveguide length of $5\lambda_g$ is used as a background and a waveguide length of $6\lambda_g$ is used as a sample. Results after ratioing the $8\lambda_g$ to the $6\lambda_g$ waveguide lengths are also shown, as well as the one sigma confidence limits of the model. The symmetry around the horizontal axis is because the poles and zeros appear as conjugate pairs. It is worth noting that the poles are similar in both cases, but

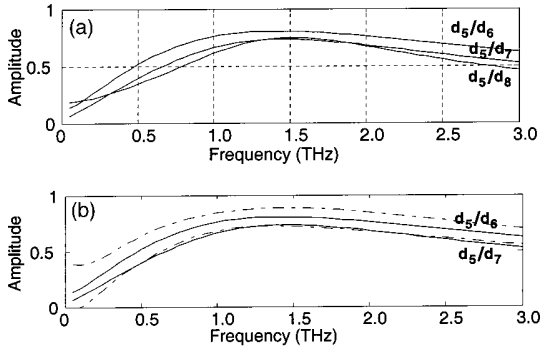

Fig. 12. (a) Calculated transmission coefficient of a waveguide of unit length of reduced height and (b) confidence levels (one sigma around the d_5/d_6 curve) of the identification procedure.

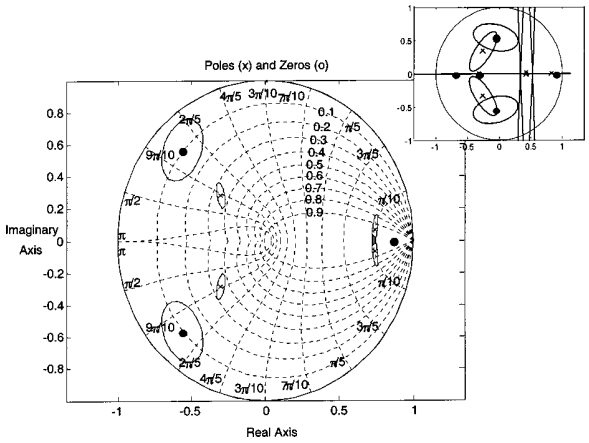

Fig. 13. Pole-zero diagram for the d_3/d_2 backshort case, with a fourth-order model. The over-parameterized sixth-order model in the inset is also shown for illustrative purposes.

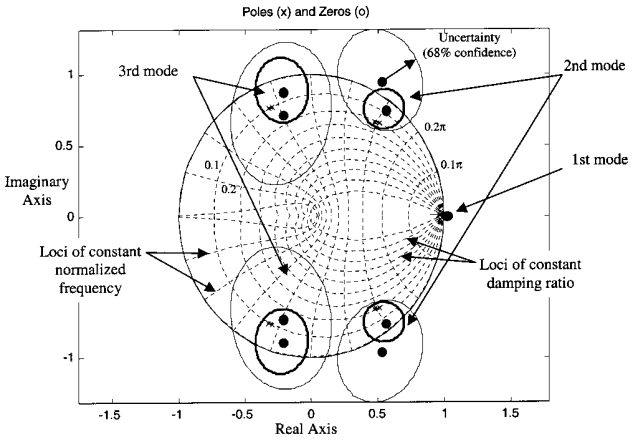

Fig. 14. Pole-zero chart of three propagating modes in an antenna-coupled reduced-height waveguide when a waveguide length of $5\lambda_g$ is used as a background and a waveguide length of $6\lambda_g$ is used as a sample (the limits of the 68% confidence loci for the zeros are represented as ellipses in a thick curve). Results after ratioing the $8\lambda_g$ to the $6\lambda_g$ waveguide lengths are also shown (in this case the confidence loci for the zeros are represented as ellipses in a thin curve).

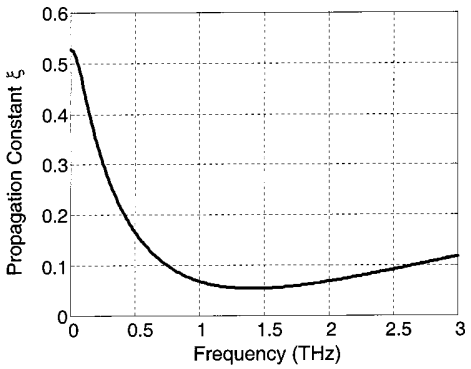

Fig. 15. Calculation of the effective (multimoded) magnitude of the propagation constant for a micromachined waveguide of unit length λ_g.

Table 1. Mode Characteristics Calculated with the ARX Model for the d_5/d_6 Data Set[a]

Mode	Poles	$\lvert w\rvert$%	f	c_1	c_2
1	0.9682; 0.9613	74.91	−0.998	−2.073	1.074
2	$0.5114 \pm 0.6539j$	6.94	1.923	−1.484	1.451
3	$-0.3235 \pm 0.7585j$	18.15	0.069	0.951	1.471

[a] Coefficients relate to Eq. (6), and mode weights are expressed as percentages of excitation.

the same is not true for the zeros. In fact, some of the zeros are outside the unit circle, which is the stability boundary in the z domain. This would imply that the corresponding mode may initially oscillate in the opposite direction of the excitation pulse ("undershoot"). However, it is possible that those zeros ended up outside the unit circle due to numerical artifacts. In fact, since their uncertainty region is large, their actual position could well be inside the circle.

At each frequency ω, the energy of a wave traveling in the waveguide is attenuated by a factor $|H(j\omega)|$ when it passes twice through a waveguide section of unit length. Hence after traveling a distance d, the energy will have decayed by a factor $|H(j\omega)|^{d/2} = \exp[\log(|H(j\omega)|^{d/2})] = \exp[-0.5d \log(|H(j\omega)|^{-1})]$. Thus the magnitude of the propagation constant at frequency ω is seen to be equal to $[\log(|H(j\omega)|^{-1})]/4$. An effective propagation constant for the multimode propagation can therefore be calculated as shown in Fig. 15. The weights of the modes assumed to be propagating in the structure calculated from the ARX model are shown in Table 1. The magnitude of the propagation constant for each mode could be inferred from each partial fraction in Eq. (6).

6. CONCLUSIONS

A quasi-optical de-embedding technique for characterizing micromachined waveguides with cut-on frequencies >100 GHz is demonstrated with wideband time-resolved terahertz spectroscopy. A transfer-function representation is adopted for the description of the relation between the signals in the input and output ports of the waveguides. The time-domain responses were discretized, and the waveguide transfer function was obtained through a parametric approach in the z domain after describing the system with an ARX model. Before the identification procedure, filtering was performed in the wavelet domain to minimize signal distortion and the noise propagating in the ARX model. The model identification procedure requires isolating the phase delay in the structure, and therefore the time-domain signatures must be first aligned with respect to each other before they are compared. The model also requires an *a priori* assumption of the number of modes propagating in the structure. An initial estimate on the number of modes propagating in the structure was provided by comparing the measured phase delay in the structure with theoretical calculations that take into account the physical dimensions of the waveguide. Parsimony arguments were also used to minimize the risk of overfitting the model parameters. Overparametrized models can be easily identified in a pole-zero diagram, as the one sigma confidence level for such models increases significantly. The direct relation between the complex insertion loss function commonly measured in THz spectroscopy and the polynomial representation of the ARX model were explicitly shown. The modeling procedure was also described within the framework of filtering. The advantages of exciting the structure with a spectrally rich source (a femtosecond pulse) were discussed within the framework of the identification procedure. Measurements for a precision WR-8 waveguide adjustable short as well as for G-band reduced-height micromachined waveguides are presented.

APPENDIX A: TREATMENT OF MULTIPLE REFLECTIONS

Any significant impedance mismatch in the antenna/waveguide structure should result in multiple-reflection signatures that would appear separated in the time domain by distances $4\bar{n}d$ as shown in Fig. 16:

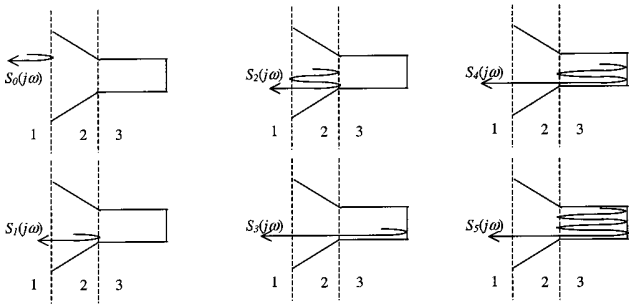

Fig. 16. Multiple reflections due to impedance mismatch between air–antenna and antenna–waveguide interfaces.

$$
\begin{aligned}
S_0(j\omega) &= P(j\omega)R_{12}(j\omega),\\
S_1(j\omega) &= P(j\omega){T_{12}}^2(j\omega)R_{23}(j\omega),\\
S_2(j\omega) &= P(j\omega){T_{12}}^2(j\omega){R_{23}}^2(j\omega)R_{12}(j\omega),\\
S_3(j\omega) &= P(j\omega){T_{12}}^2(j\omega){T_{23}}^2(j\omega)H(j\omega),\\
S_4(j\omega) &= P(j\omega){T_{12}}^2(j\omega){T_{23}}^2(j\omega)R_{23}(j\omega)H^2(j\omega).
\end{aligned}
\tag{A1}
$$

After estimating $H(j\omega)$ by inserting different waveguide lengths, the fractions

$$
\frac{S_0(j\omega)}{S_1(j\omega)}, \quad \frac{S_2(j\omega)}{S_1(j\omega)}, \quad \frac{S_3(j\omega)}{S_2(j\omega)}, \quad \frac{S_4(j\omega)}{S_3(j\omega)}
$$

can be used to calculate $R_{12}(j\omega)$, $R_{23}(j\omega)$, $T_{12}(j\omega)$, $T_{23}(j\omega)$. These fractions can be obtained by ARX parametric identification; that is, instead of ratioing $S_{i+1}(j\omega)$ against $S_i(j\omega)$, we are identifying a linear system that has an output $y(t) = s_{i+1}(t)$ for an input $u(t) = s_i(t)$. One can also write

$$
H(j\omega) = \frac{S_5(j\omega)}{S_4(j\omega)} \frac{1}{R_{23}(j\omega)} \tag{A2}
$$

to obtain a new estimate of $H(j\omega)$ from the multiple-reflection signatures $S_4(j\omega)$ and $S_5(j\omega)$. If this new estimate is substantially different from the one originally obtained, the process of estimating $R_{12}(j\omega)$, $R_{23}(j\omega)$, $T_{12}(j\omega)$, and $T_{23}(j\omega)$ would be repeated.

APPENDIX B: ANALOGY BETWEEN AN AUTOREGRESSIVE WITH EXOGENOUS INPUT MODEL AND A DISPERSIVE FOURIER-TRANSFORM SPECTROMETER

With reference to Eq. (5), dropping the z^{-k} term and factorizing the denominator,

$$
H(z) = \sum_{i=1}^{n+m} w_i \frac{1 + f_i z^{-1}}{(1 - p_{i1}z^{-1})(1 - p_{i2}z^{-1})}, \tag{B1}
$$

where $\{p_{i1}, p_{i2}\}$, $i = 1 \ldots n_a/2$, are the roots (the poles of the transfer function) of $D(z)$. Let $\Lambda_i(z) = H(z)(1 - p_{i1}z^{-1})(1 - p_{i2}z^{-1})$; then $\Lambda_i(p_{i1}) = w_i(1 + f_i p_{i1}^{-1})$, since all other terms vanish if there are no multiple poles. Similarly, $\Lambda_i(p_{i2}) = w_i(1 + f_i p_{i2}^{-1})$, and therefore a system of two equations with two unknowns (w_i and f_i) can be solved. Setting

$$
\begin{aligned}
H(z)\big|_{z=\exp(j\omega T_s)} &= \sum_{i=1}^{n+m} w_i \frac{1 + f_i \exp(-j\omega T_s)}{1 + c_{i1}\exp(-j\omega T_s) + c_{i2}\exp(-2j\omega T_s)}\\
&= \sum_{i=1}^{n+m} (\alpha_i + j\beta_i) = A\exp(j\phi),
\end{aligned}
\tag{B2}
$$

it follows that

$$
H(j\omega) = \sum_{i=1}^{n+m} w_i \frac{[1 + f_i\cos(\omega T_s)] - jf_i\sin(\omega T_s)}{[1 + c_{i1}\cos(\omega T_s) + c_{i2}\cos(2\omega T_s)] - j[c_{i1}\sin(\omega T_s) + c_{i2}\sin(2\omega T_s)]}, \tag{B3}
$$

$$
A = \sqrt{\left(\sum_{i=1}^{m+n}\alpha_i\right)^2 + \left(\sum_{i=1}^{m+n}\beta_i\right)^2}, \tag{B4}
$$

$$
\phi = a\tan\left(\sum_{i=1}^{m+n}\beta_i \Big/ \sum_{i=1}^{m+n}\alpha_i\right), \tag{B5}
$$

$$
\alpha_i = w_i \frac{[1 + f_i\cos(\omega T_s)][1 + c_{i1}\cos(\omega T_s) + c_{i2}\cos(2\omega T_s)] + f_i\sin(\omega T_s)[c_{i1}\sin(\omega T_s) + c_{i2}\sin(2\omega T_s)]}{[1 + c_{i1}\cos(\omega T_s) + c_{i2}\cos(2\omega T_s)]^2 + [c_{i1}\sin(\omega T_s) + c_{i2}\sin(2\omega T_s)]^2}, \tag{B6}
$$

$$
\beta_i = w_i \frac{[1 + f_i\cos(\omega T_s)][c_{i1}\sin(\omega T_s) + c_{i2}\sin(2\omega T_s)] - f_i\sin(\omega T_s)[1 + c_{i1}\cos(\omega T_s) + c_{i2}\cos(2\omega T_s)]}{[1 + c_{i1}\cos(\omega T_s) + c_{i2}\cos(2\omega T_s)]^2 + [c_{i1}\sin(\omega T_s) + c_{i2}\sin(2\omega T_s)]^2}. \tag{B7}
$$

This formulation of the problem directly relates the ARX model identification procedure to the more familiar equations for the complex insertion loss commonly used in DFTS.

APPENDIX C: AUTOREGRESSIVE WITH EXOGENOUS INPUT IDENTIFICATION PROCEDURE

Let $y[k]$ and $u[k]$, $\{k = 1 \ldots N\}$, be the signals measured for the longer and shorter waveguides, respectively. Let also

$$
\boldsymbol{\theta} = [-a_1 \ -a_2 \ \cdots \ -a_{n_a} \ b_1 \ b_2 \ \cdots \ b_{n_b}]^T \tag{C1}
$$

(where T signifies the transpose) be the vector of model coefficients and

$$\mathbf{\Phi}_{(N-n_a)\times(n_a+n_b)} = \begin{bmatrix} y[n_a] & y[n_a-1] & \cdots & y[1] & u[n_a] & u[n_a-1] & \cdots & u[n_a-n_b+1] \\ y[n_a+1] & y[n_a] & \cdots & y[2] & u[n_a+1] & u[n_a] & \cdots & u[n_a-n_b+2] \\ \vdots & \vdots & \cdots & \vdots & \vdots & \vdots & \cdots & \vdots \\ y[N-1] & y[N-2] & \cdots & y[N-n_a] & u[N-1] & u[N-2] & \cdots & u[N-n_b] \end{bmatrix} \quad \text{(C2)}$$

be the matrix of regressors. It is then possible to write $\hat{\mathbf{y}} = \mathbf{\Phi}\boldsymbol{\theta}$, where

$$\hat{\mathbf{y}}_{(N-n_a)\times 1} = [\hat{y}[n_a+1]\ \hat{y}[n_a+2]\ \cdots\ \hat{y}[N]]^T, \quad \text{(C3)}$$

where the hat denotes an estimated value. In this manner, a vector of prediction errors can be written as $\boldsymbol{\epsilon} = \mathbf{y} - \mathbf{\Phi}\boldsymbol{\theta}$, where

$$\mathbf{y}_{(N-n_a)\times 1} = [y[n_a+1]\ y[n_a+2]\ \cdots\ y[N]]^T. \quad \text{(C4)}$$

Least-squares estimation consists of minimizing the sum of the squared errors, given by $\mathbf{J} = \boldsymbol{\epsilon}^T\boldsymbol{\epsilon}$, with respect to $\boldsymbol{\theta}$ (i.e., $\partial\mathbf{J}/\partial\boldsymbol{\theta} = 0$). The result is the least-squares estimate of $\boldsymbol{\theta}$, denoted by $\hat{\boldsymbol{\theta}}$, which is obtained as $\hat{\boldsymbol{\theta}} = (\mathbf{\Phi}^T\mathbf{\Phi})^{-1}\mathbf{\Phi}^T\mathbf{y}$, provided $\mathbf{\Phi}^T\mathbf{\Phi}$ is nonsingular. The standard error of the estimate $\hat{\boldsymbol{\theta}}$ is given by the square root of the diagonal elements of matrix $\mathbf{S}$, given by

$$\mathbf{S} = (\mathbf{\Phi}^T\mathbf{\Phi})^{-1}\left[\frac{(\mathbf{y}-\hat{\mathbf{y}})^T(\mathbf{y}-\hat{\mathbf{y}})}{(N-n_a)-(n_a+n_b)}\right], \quad \text{(C5)}$$

where $\hat{\mathbf{y}} = \mathbf{\Phi}\hat{\boldsymbol{\theta}}$. The term in square brackets in Eq. (C5) is the square of the standard error of the estimate for y, adjusted for the number of observations $(N - n_a)$ in the time domain and estimated variables $(n_a + n_b)$. It is worth noting that the influence of noise in the estimation process will be reduced if there is not too much collinearity between the columns of $\mathbf{\Phi}$. This translates into the following requirements:

(a) The length of the waveguide inserted must be large enough to produce a detectable difference between signals y and u.

(b) The values of u should not be strongly correlated to their past values. This is ensured if u has a rich spectral content. For instance, if u is a sinusoid, $u[k]$ is a linear combination of $u[k-1]$ and $u[k-2]$, for all k. If u is a combination of sinusoids of two different frequencies, $u[k]$ is a linear combination of $u[k-1],\ldots,u[k-4]$. It is then seen that, the larger the number of frequencies present at u, the larger the number of columns that can be placed in the u part of $\mathbf{\Phi}$.

(c) The values of y should not be strongly correlated to their past values. Correlations of this sort can arise, even if u is spectrally rich, because the system may filter out some frequencies (low-pass action). Problems may then arise if the number of columns in the y part of $\mathbf{\Phi}$ (model order n_a) is too large (overparametrization).

ACKNOWLEDGMENTS

S. Hadjiloucas and H. P. M. Pellemans would like to acknowledge financial support from the European Community through the Training and Mobility of Researchers grant FMRX-CT96-0092. R. K. H. Galvão was supported by Fundação de Amparo à Pesquisa do Estado de São Paulo under postdoctorate grant 00/09390-6.

REFERENCES

1. R. W. Beatty, G. F. Engen, and W. J. Anson, "Measurement of reflection and losses of waveguide joints and connectors using microwave reflectometer techniques," IRE Trans. Instrum. **9**, 219–226 (1960).
2. G. F. Engen, "An extension to the sliding short method of connector and adapter evaluation," J. Res. Natl. Bur. Stand. **75**, 177–183 (1971).
3. M. P. Weidman, "A semi-automated six port for measuring millimeter-wave power and complex reflection coefficient," IEEE Trans. Microwave Theory Tech. **25**, 1083–1085 (1977).
4. G. F. Engen, "The six port reflectometer: an alternative network analyzer," IEEE Trans. Microwave Theory Tech. **25**, 1075–1083 (1977).
5. G. F. Engen, "A (historical) review of the six-port measurement technique," IEEE Trans. Microwave Theory Tech. **45**, 2414–2417 (1997).
6. G. F. Engen, "Calibration of an arbitrary six-port junction for measurement of active and passive circuit parameters," IEEE Trans. Instrum. Meas. **22**, 295–299 (1973).
7. G. F. Engen, "Calibrating the six-port reflectometer by means of sliding terminations," IEEE Trans. Microwave Theory Tech. **26**, 951–957 (1978).
8. T. E. Hodgetts, "A numerically stable algorithm for calibrating single six-ports for national microwave reflectometry," NPL Rep. DES 102 (National Physical Laboratory, Teddington, UK, 1990).
9. H. J. Eul and B. Schiek, "A generalized theory and new calibration procedures for network analyzer self-calibration," IEEE Trans. Microwave Theory Tech. **39**, 724–731 (1991).
10. K. J. Silvonen, "A general approach to network analyzer calibration," IEEE Trans. Microwave Theory Tech. **40**, 754–759 (1992).
11. G. F. Engen and C. A. Hoer, "Thru-Reflect-Line: an improved technique for calibrating the dual six-port automatic network analyzer," IEEE Trans. Microwave Theory Tech. **27**, 987–993 (1979).
12. G. F. Engen, "Calibration technique for automated network analyzers with application to adapter evaluation," IEEE Trans. Microwave Theory Tech. **22**, 1255–1260 (1974).
13. C. A. Hoer, "Performance of a dual six port network analyzer," IEEE Trans. Microwave Theory Tech. **27**, 993–998 (1979).
14. B. Knudsen, G. F. Engen, and B. Guldbrandsen, "Accuracy assessment of the scalar network analyzer using sliding termination techniques," IEEE Trans. Instrum. Meas. **38**, 480–483 (1989).
15. D. J. Bannister, E. J. Griffin, and T. E. Hodgetts, "On the dimensional tolerances of rectangular waveguide for reflectometry at millimetric wavelengths," NPL Rep. DES 95 (National Physical Laboratory, Teddington, UK, 1989).
16. J. R. Birch and R. N. Clarke, "Dielectric and optical measurements from 30 to 1000 GHz," J. Inst. Electron. Rad. Eng. **52**, 565–584 (1982).
17. L. C. Oldfield, J. P. Ide, and E. J. Griffin, "A multistate reflectometer," IEEE Trans. Instrum. Meas. **25**, 198–201 (1985).
18. D. Thompson, R. D. Pollard, and R. E. Miles, "One-port

S-parameter measurements using quasi-optical multistate reflectometer," Electron. Lett. **34**, 1222–1224 (1998).
19. S. Hadjiloucas, J. W. Bowen, J. W. Digby, J. M. Chamberlain, and D. P. Steenson, "Quasi-optical characterization of waveguides at frequencies above 100 GHz," J. M. Chamberlain and P. Harrison, eds., *Conference on Terahertz Spectroscopy and Applications, Munich*, Proc. SPIE **3828**, 357–365 (1999).
20. J. W. Bowen, S. Hadjiloucas, and L. S. Karatzas, "Characteristic impedance measurements of a WR-10 waveguide sample with a dispersive Fourier transform spectrometer," in *Applied Optics and Optoelectronics*, A. T. Augousti, ed. (Institute of Physics, Bristol, UK, 1998), pp. 181–186.
21. J. W. Digby, C. E. McIntosh, G. M. Parkhurst, B. M. Towlson, S. Hadjiloucas, J. W. Bowen, J. M. Chamberlain, R. D. Pollard, R. E. Miles, D. P. Steenson, L. S. Karatzas, N. J. Cronin, and S. R. Davies, "Fabrication and characterization of micro-machined rectangular waveguide components for use at millimeter wave and terahertz frequencies," IEEE Trans. Microwave Theory Tech. **48**, 1293–1303 (2000).
22. R. W. McGowan, G. Gallot, and D. Grischkowsky, "Propagation of ultra-wideband, short Pulses of THz radiation through sub-mm diameter circular waveguides," Opt. Lett. **24**, 1431–1433 (1999).
23. G. Gallot, S. P. Jamison, R. W. McGowan, and D. Grischkowsky, "THz waveguides," J. Opt. Soc. Am. B **17**, 851–863 (2000).
24. D. Grischkowsky, "Optoelectronic characterization of transmission lines and waveguides by THz time-domain spectroscopy," IEEE J. Sel. Top. Quantum Electron. **6**, 1122–1135 (2000).
25. S. P. Jamison, R. W. McGowan, and D. Grischkowsky, "Single-mode waveguide propagation and reshaping of sub-ps terahertz pulses in sapphire fibers," Appl. Phys. Lett. **76**, 1987–1989 (2000).
26. R. Mendis and D. Grischkowsky, "Plastic ribbon THz waveguides," J. Appl. Phys. **88**, 4449–4451 (2000).
27. R. Mendis and D. Grischkowsky, "Undistorted guided wave propagation of subpicosecond THz pulses," Opt. Lett. **26**, 846–848 (2001).
28. P. R. Smith, D. H. Auston, and M. C. Nuss, "Subpicosecond photoconducting dipole antennas," IEEE J. Quantum Electron. **24**, 255–260 (1988).
29. M. C. Nuss and J. Orenstein, "Millimeter and submillimeter wave spectroscopy of solids," in *Topics Current Chemistry*, E. Grüner, ed. (Springer-Verlag, Heidelberg 1998), Vol. 74, pp. 7–50.
30. P. Haring Bolivar, "Coherent THz spectroscopy," in *Semiconductor Quantum Optoelectronics: From Quantum Physics to Smart Devices*, A. Miller, M. Ebrahimzahdeh, and D. M. Finlayson, eds. (Institute of Physics, Bristol, UK, 1999), Chap. 5, pp. 151–192.
31. P. Haring Bolívar, M. Brucherseifer, H. P. M. Pellemans, and H. Kurz, "Time domain THz spectroscopy and sensing," in *THz Sources and Systems*, R. E. Miles, P. Harrison, and D. Lippens, eds. (Kluwer Academic, Dordrecht, The Netherlands, 2001), pp. 315–328.
32. S. M. Kay and S. L. Marple, Jr., "Spectrum analysis, a modern perspective," Proc. IEEE **69**, 1380–1419 (1981).
33. S. T. D. Dorney, R. G. Barasniuk, and D. M. Mittleman, "Material parameter estimation with terahertz time-domain spectroscopy," J. Opt. Soc. Am. A **18**, 1562–1571 (2001).
34. L. Ljung, *System Identification, Theory for the User*, 2nd ed. (Prentice Hall, Upper Saddle River, N.J., 1999).
35. J. R. Birch and T. J. Parker, "Dispersive Fourier transform spectrometry," in *Infrared and Millimeter Waves*, K. J. Button, ed. (Academic, Orlando, Fla., 1979), Vol. 2, Chap. 3, pp. 137–271.
36. N. Marcuvitz, *Waveguide Handbook* (Peregrinus, London, 1993).
37. I. Daubechies, *Ten Lectures on Wavelets* (Society for Industrial and Applied Mathematics, Philadelphia, 1992).
38. M. Misiti, Y. Misiti, G. Oppenheim, and J. M. Poggi, *Wavelet Toolbox User's Guide* (Mathworks, Natick, Mass., 1996).
39. S. G. Mallat, "A theory for multiresolution signal decomposition: the wavelet representation," IEEE Pattern Anal. **11**, 674–693 (1989).
40. H. Krim, D. Tucker, S. G. Mallat, and D. Donoho, "On denoising and best signal representation," IEEE Trans. Inf. Theory **45**, 2225–2238 (1999).
41. I. Daubechies, S. Mallat, and A. S. Willsky, "Special issue on wavelet transforms and multiresolution signal analysis: introduction," IEEE Trans. Inf. Theory **38**, 529–531 (1992).
42. S. Qian and D. Chen, *Joint Time-Frequency Analysis—Methods and Applications* (Prentice-Hall, Upper Saddle River, N.J., 1996).
43. U. L. Pen, "Application of wavelets to filtering of noisy data," Philos. Trans. R. Soc. London, Ser. A **357**, 2561–2571 (1999).